Electronic Supplementary Material (ESI) for Journal of Materials Chemistry A.

Promising Nano-Silicon Anodes Prepared by the "Disperse-Anchor" Strategy and Functional Carbon Nanotube Interlayers for Flexible Lithium-Ion Batteries

Zixin Hong[a], Zhenhan Fang[a,*], Yufeng Luo[b], Hengcai Wu[a], Hui Tian[a], Fei Zhao[a], Qunqing Li[a, c], Shoushan Fan[a], and Jiaping Wang[a, c,*]

[a] *Department of Physics and Tsinghua-Foxconn Nanotechnology Research Center, Tsinghua University, Beijing, 100084, China*
[b] *Institute of Textiles and Clothing, Hong Kong Polytechnic University, Hong Kong, China*
[c] *Frontier Science Center for Quantum Information, Beijing, 100084, China*
[*]Corresponding author.
E-mail address:
fzh17@mails.tsinghua.edu.cn (Zhenhan Fang)
jpwang@tsinghua.edu.cn (Jiaping Wang)

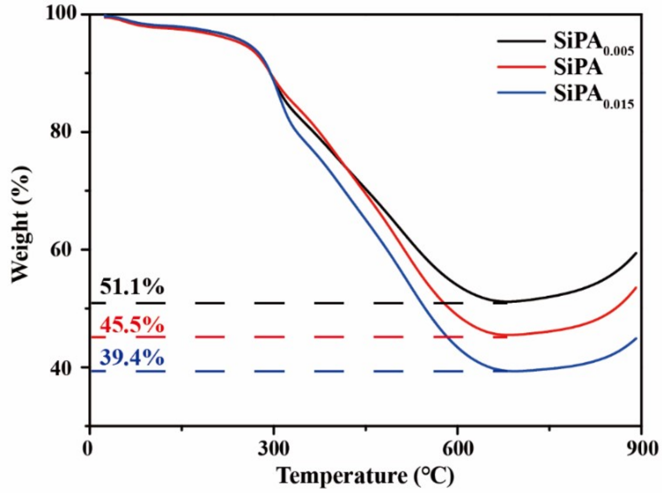

Fig. S1 The TGA curves of $SiPA_{0.005}$, SiPA, and $SiPA_{0.015}$.

Fig. S1 shows the TGA curves of the samples with different amounts of PANI coating. The mass percentages of Si for $SiPA_{0.005}$, SiPA, and $SiPA_{0.015}$ are 51.1%, 45.5%, and 39.4%, respectively. The increase of sample mass at high temperature is due to the oxidation of Si.

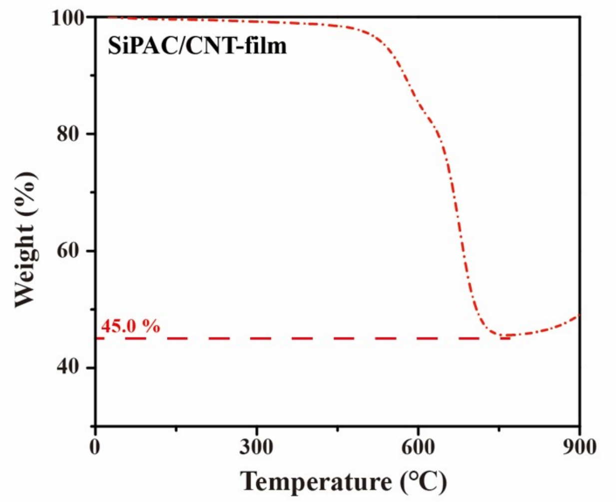

Fig. S2 TGA curve of the SiPAC/CNT-film.

Fig. S2 presents the TGA curve of the SiPAC/CNT-film. The mass content of Si in the SiPAC/CNT-film is about 45%.

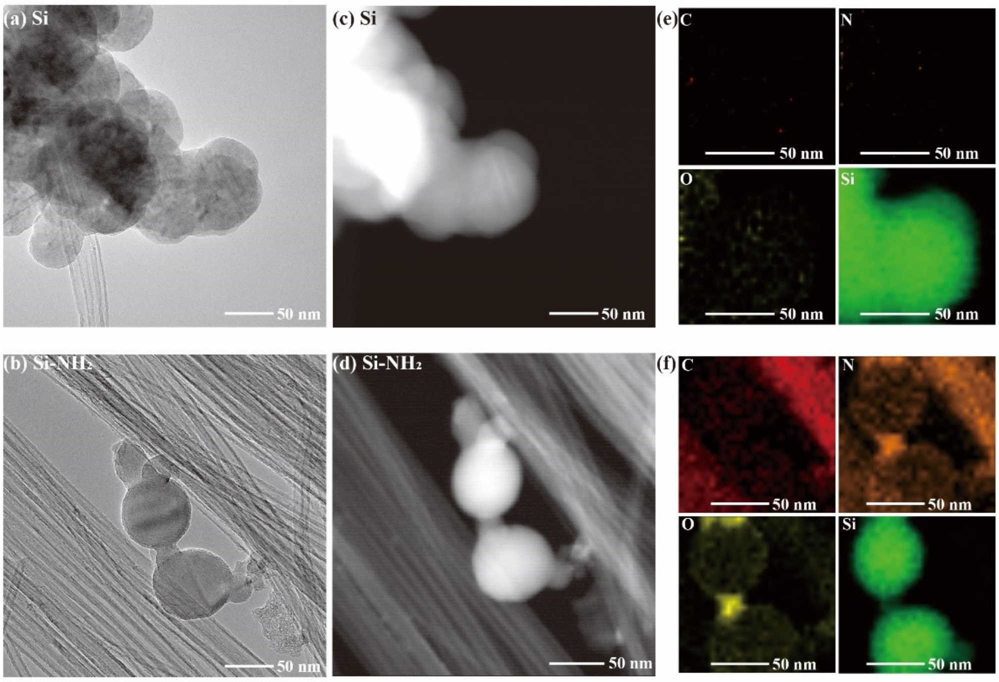

Fig. S3 TEM, STEM, and EDS elemental mapping of (a,c,e) Si and (b,d,f) Si-NH_2.

Fig. S3a shows large clusters of Si. The energy-dispersive spectroscopy (EDS) element mapping of C, N, O, and Si in Si and Si-NH2 are shown in Fig. S3e, f. For Si, there are almost no C and N elements, and the small amount of O element may be derived from the surface Si oxides. For Si-NH2, a clear distribution of Si, N, and O elements is observed, suggesting successful surface modification.

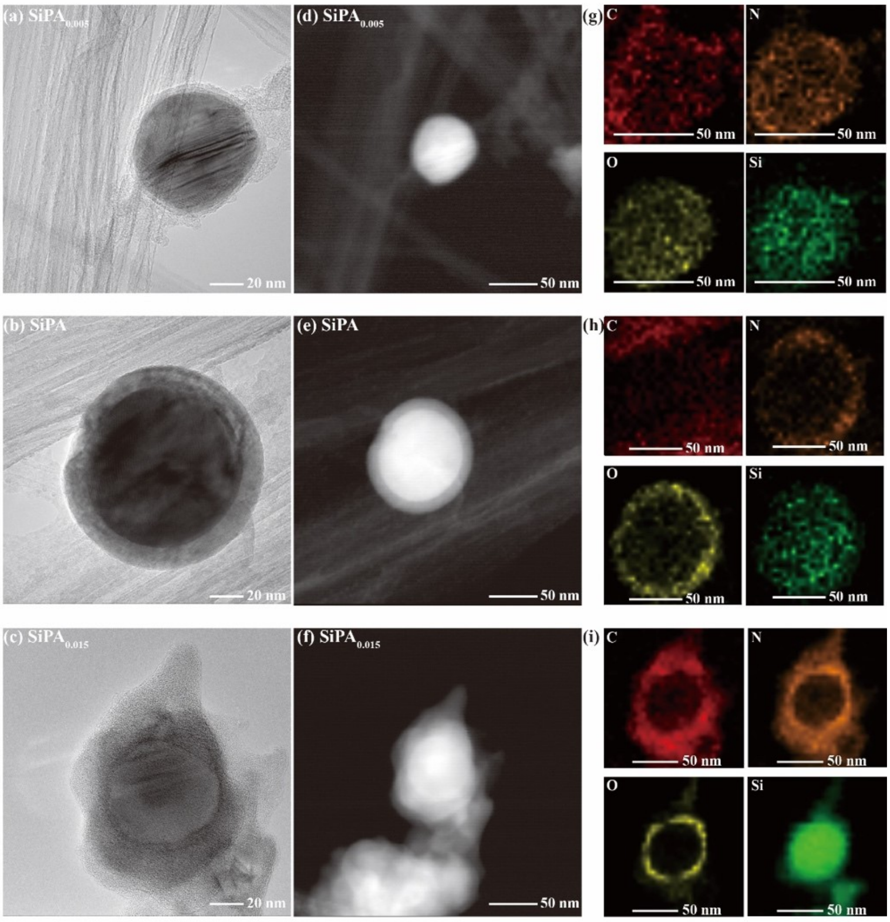

Fig. S4 TEM images of Si samples with different amounts of PANI coating: (a) $SiPA_{0.005}$, (b) SiPA, (c) $SiPA_{0.015}$. STEM images of (d) $SiPA_{0.005}$, (e) SiPA, (f) $SiPA_{0.015}$. EDS elemental mapping images of (g) $SiPA_{0.005}$, (h) SiPA, (i) $SiPA_{0.015}$.

TEM and Scanning TEM (STEM) images of $SiPA_{0.005}$, SiPA, and $SiPA_{0.015}$ are presented in Fig. S4a-c and d-f, respectively, where the thickness of the PANI coating layer increases with the increase of the aniline amount.

The EDS element mapping images for C, N, O, and Si are shown in Fig. S4g-i. For $SiPA_{0.005}$, the distribution of the four elements is uniform (Fig. S4g), which may be due to the thin PANI layer. For SiPA (Fig. S4h) and $SiPA_{0.015}$ (Fig. S4i), Si is centered and C, N, and O are spread in the external layer.

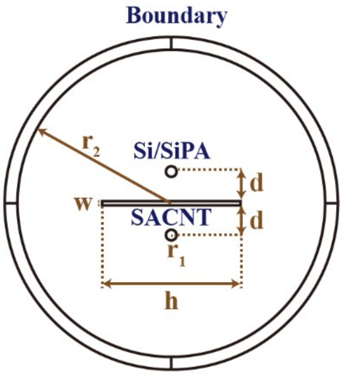

Fig. S5 Model diagram of the finite element simulation.

Fig. S5 shows the finite element calculation model simulating the dispersion of particles and SACNT, where the rectangle represents SACNT, the two small circles refer to the particles (Si or SiPA), the inner large circle refers to the adjacent solution range, and the outer large circle indicates the solution boundary at infinity where the potential is zero. The specific parameters and their meanings are shown in Table S1.

Table S1. Parameters of finite element model.

Parameter	Description	Value
r_1	Radius of particles	40 nm (Si) 50 nm (SiPA)
r_2	Distance from the center of SACNT to the boundary of the domain calculation range	1.2 μm
h	Length of SACNT	1 μm
w	Diameter of SACNT	30 nm
d	Distance from particle to SACNT	250 nm
φ_1	Zeta potential of the particle	-3.9 mV (Si) +6.4 mV (SiPA)
φ_2	Zeta potential of SACNT	-1.6 mV

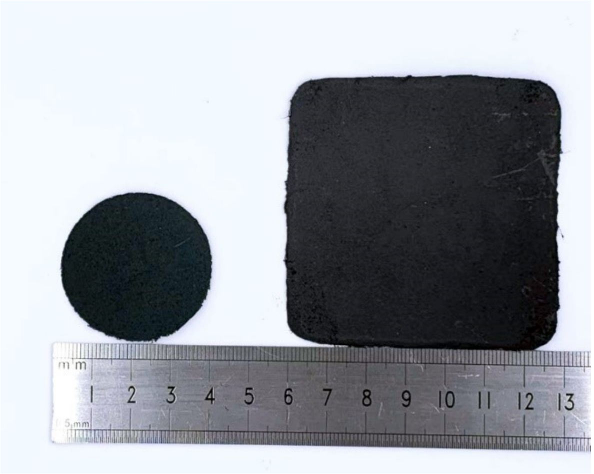

Fig. S6 SiPA/CNT films with different sizes and shapes obtained by vacuum filtration.

By modifying the molds for vacuum filtration, different sizes and shapes of SiPA/CNT films can be produced.

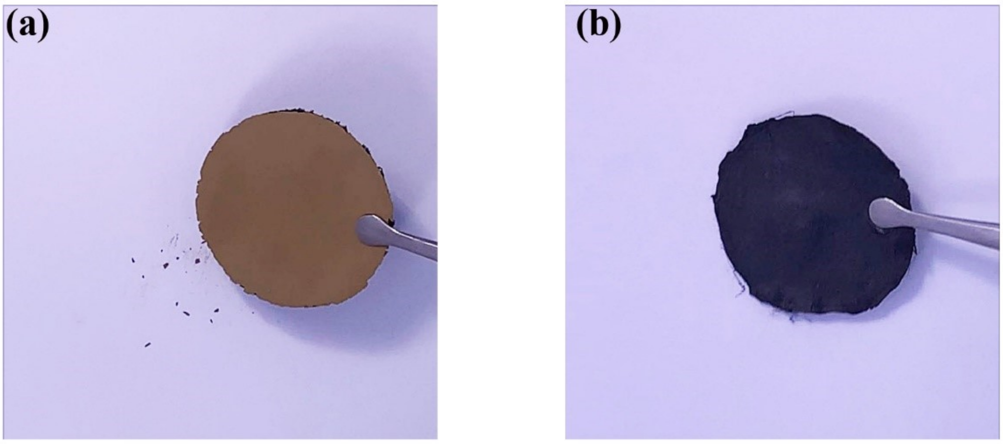

Fig. S7 (a) Active material shedding of Si/CNT and (b) stable structure of Si/CNT-film upon shaken.

The active material of the Si/CNT sample detaches easily from the anode when shaken (Fig. S7a, Video S3), while the Si/CNT-film with the functional CNT film structure remains structural integrity (Fig. S7b, Video S4).

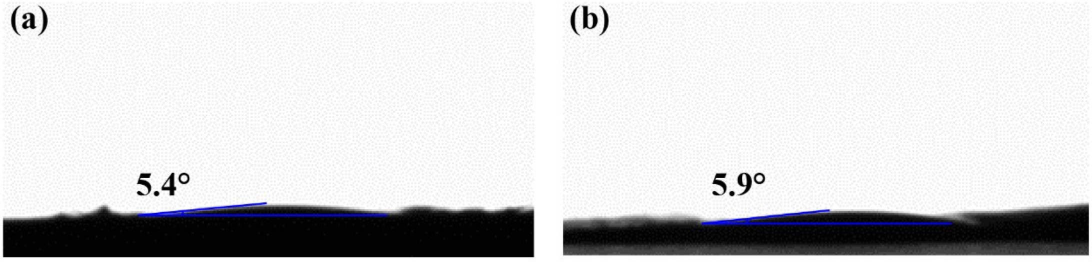

Fig. S8 The wetting behaviors of (a) SiPAC/CNT and (b) SiPAC/CNT-film.

Both SiPAC/CNT and SiPAC/CNT-film show excellent wettability to organic solvent droplets, indicating that the functional CNT layer does not hinder the penetration of the organic solvent into electrodes.

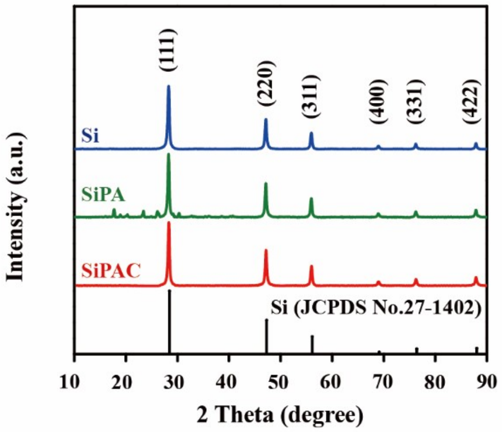

Fig. S9 XRD pattern of Si, SiPA, and SiPAC.

Fig. S9 presents the XRD patterns of Si, SiPA, and SiPAC powders. The lattice structure of Si remains during the surface treatments. In the XRD results of SiPA powders, there are many small chaotic peaks around 20°, which are ascribed to PANI [1, 2]. In addition, there is no information about silicon oxides in the XRD curves of Si, SiPA, and SiPAC.

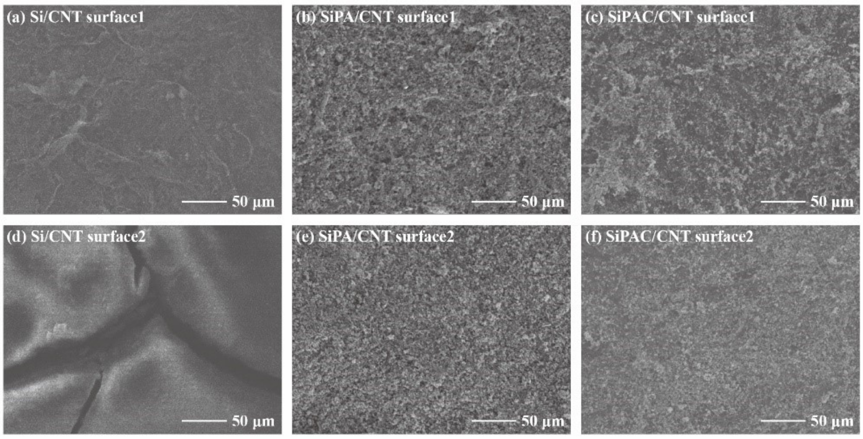

Fig. S10 SEM images of the surface of the Si/CNT, SiPA/CNT, and SiPAC/CNT anodes.

The surface SEM of the Si/CNT anode reveals that one side of it is mainly CNT (Fig. S10a), while the other side is mainly Si (Fig. S10d). It indicates that the Si/CNT anode is severely delaminated, which is consistent with the cross-section SEM image (Fig. 1h). The surface SEMs of SiPA/CNT and SiPAC/CNT anodes are presented in Fig. S10b, e and Fig. S10c, f, respectively. For SiPA/CNT and SiPAC/CNT anodes, the active material and CNT are uniformly dispersed, which is in accordance with the cross-section SEM image (Fig. 1i).

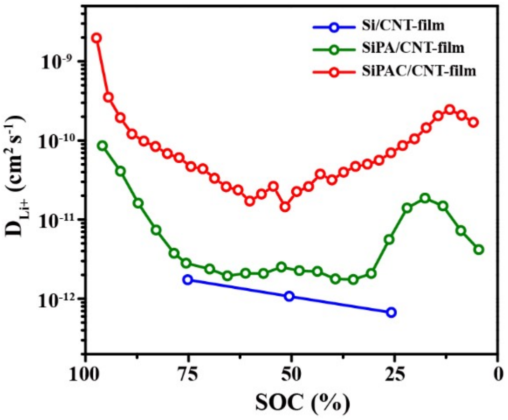

Fig. S11 $D_{Li}{}^{+}$ of the Si/CNT-film, SiPA/CNT-film, and SiPAC/CNT-film anodes based on the second de-lithiation process.

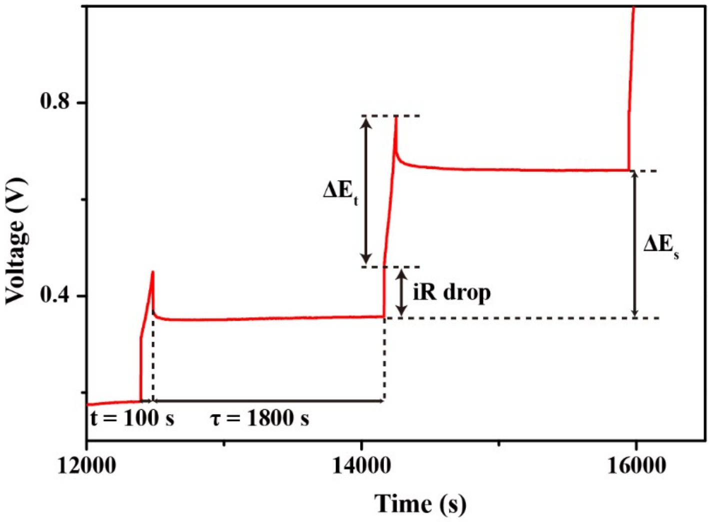

Fig. S12 Illustration of the GITT calculation.

Fig. S12 presents a local magnification of the GITT (in the first test, 1 A g^{-1}, pulse time 100 s, relaxation time 1800 s) and the lithium-ion diffusion coefficient $D_{Li}{}^{+}$ is calculated using the following equation:[1]

$$D_{Li}^{+} = \frac{4}{\pi\tau}\left(\frac{m_B V_M}{M_B S}\right)^2\left(\frac{\Delta E_s}{\Delta E_t}\right)^2 \#(Eq.\,A1)$$

In this equation, τ is the relaxation time (s), m_B is the mass of the active material (g), M_B is the molar mass of the active material (g mol^{-1}), V_M is the molar volume of the active material (cm^3 mol^{-1}), S is the area of the electrode (cm^2), ΔE_s is the steady-state voltage change due to the current pulse (V), and ΔE_t is the voltage change after an internal iR drop in a current pulse (V).

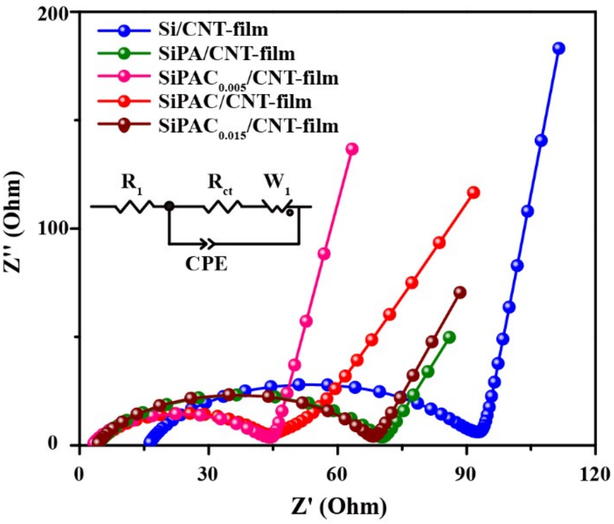

Fig. S13 EIS curves of different anodes and the equivalent circuit.

Based on the equivalent circuit shown in Fig. S13, the EIS curves for different anodes are fitted to obtain R_1 of 16.0, 4.1, 3.1, 4.1, 4.0 Ω, and R_{ct} of 74.2, 66.5, 39.4, 36.6, 64.6 Ω for the Si/CNT-film, SiPA/CNT-film, $SiPAC_{0.005}$/CNT-film, SiPAC/CNT-film, and CNT@$SiPAC_{0.015}$/CNT-film anodes, respectively. Surface coating with PANI and high-temperature carbonization can improve the interfacial contact between Si and electrolyte and reduce the resistance.

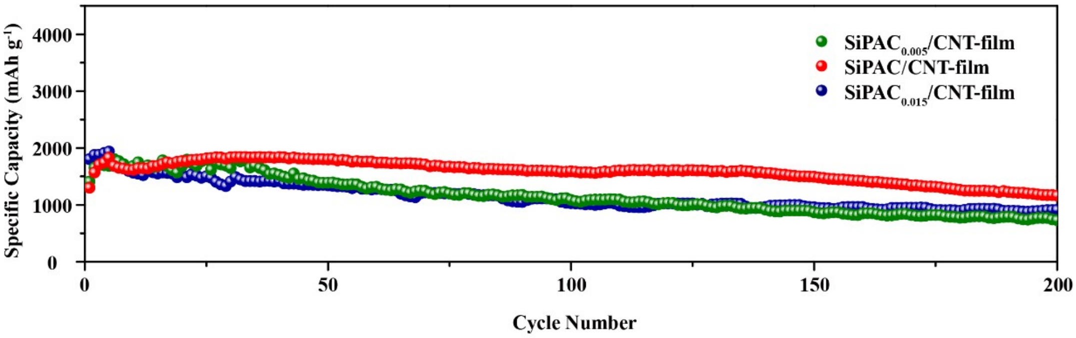

Fig. S14 Cycling performances of anodes with different PANI coating amounts.

The initial specific capacities of the SiPAC$_{0.005}$/CNT-film, SiPAC/CNT-film, and SiPAC$_{0.015}$/CNT-film anodes are 1409.2, 1302.5, and 1803.0 mAh g^{-1}, respectively. After 200 cycles at 0.4 A g^{-1}, the specific capacities of the three anodes are 731.1, 1164.5, and 910.6 mAh g^{-1} in order.

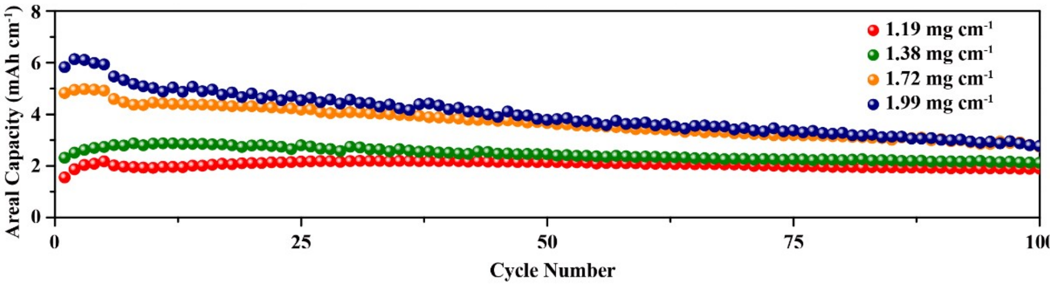

Fig. S15 Cycling performances of SiPAC/CNT-film anodes with different mass loadings.

For anodes with the loading of 1.19, 1.38, 1.72, and 1.99 mg cm^{-2} of Si, the areal capacities are 1.55, 2.31, 4.83, and 5.83 mAh cm^{-2} in the first charge/discharge cycle, and remain 1.90, 2.12, 2.74, and 2.77 mAh cm^{-2} after 100 cycles at a current density of 0.4 A g^{-1}, respectively.

Table S2 Areal specific capacities of SiPAC/CNT-film anodes with different areal loadings and comparison with data in the literature at the 100th cycle.

Sample	**Current density (A g^{-1})**	**Areal loading (mg cm^{-2})**	**Areal specific capacity at the 100th cycle (mAh cm^{-2})**	**Reference**
3D NPC@Si	0.50	0.6	0.94	[3]
Si/N-doped C/CNT	0.50	0.8-1.0	0.83-1.03	[4]
C/Si/polymer	0.10	1	0.72	[5]
CLP-Si/C	0.25	1	0.99	[6]
Si/CNT/C	1.00	1	1.39	[7]
Si@C	0.50	1	1.50	[8]
Si/nano-Cu/CNTs/C	0.20	0.85-1.18	0.98-1.35	[9]
Si/rGO/C	0.84	1.1	1.60	[10]
Si/C	0.50	1.22	1.55	[11]
PSi/C	0.10	1.27	1.19	[12]
Si/$NiSi_2/SiC$/C	0.20	2	2.6	[13]
SiPAC/CNT-film	0.40	1.99	2.77	This work

Table S3 The specific capacities of Si/CNT-film and SiPAC/CNT-film based on the masses of Si and electrode.

Anode	Specific capacity of the 1st cycle (based on Si) (mAh g^{-1})	Specific capacity of the 1st cycle (based on electrode) (mAh g^{-1})	Specific capacity of the 200th cycle (based on Si) (mAh g^{-1})	Specific capacity of the 200th cycle (based on electrode) (mAh g^{-1})
Si/CNT-film	1355.1	1016.3	188.7	141.5
SiPAC/CNT-film	1302.5	586.1	1164.5	524.0

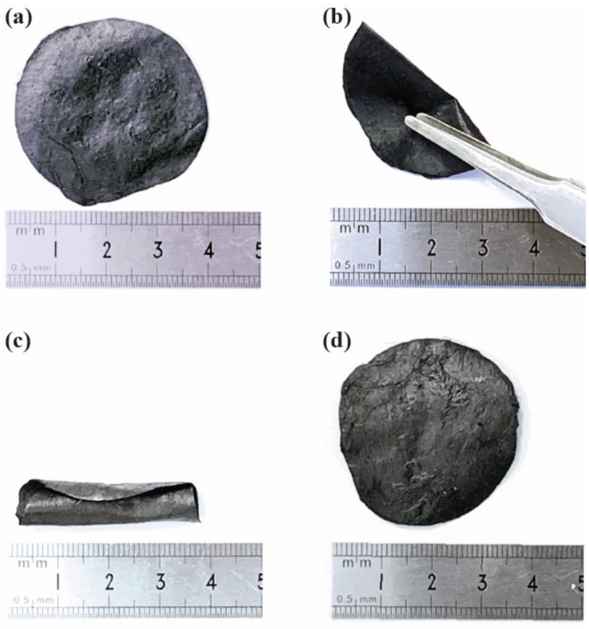

Fig. S16 Optical photos of the SiPAC/CNT-film in (a) flat, (b) 180° bent, (c) rolled, and (d) recovered states.

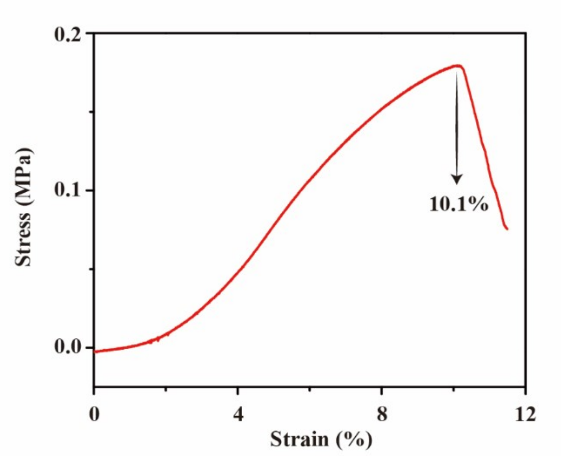

Fig. S17 Stress-strain curve of the SiPAC/CNT-film.

The stress-strain curve of the SiPAC/CNT-film in Fig. S17 shows that it can withstand 10.1% tensile strain and the Young's modulus of the film is 1.77 MPa. The SiPAC/CNT-film performs well in bending flexibility. However, the tensile flexibility remains to be improved, which will be considered in our subsequent work.

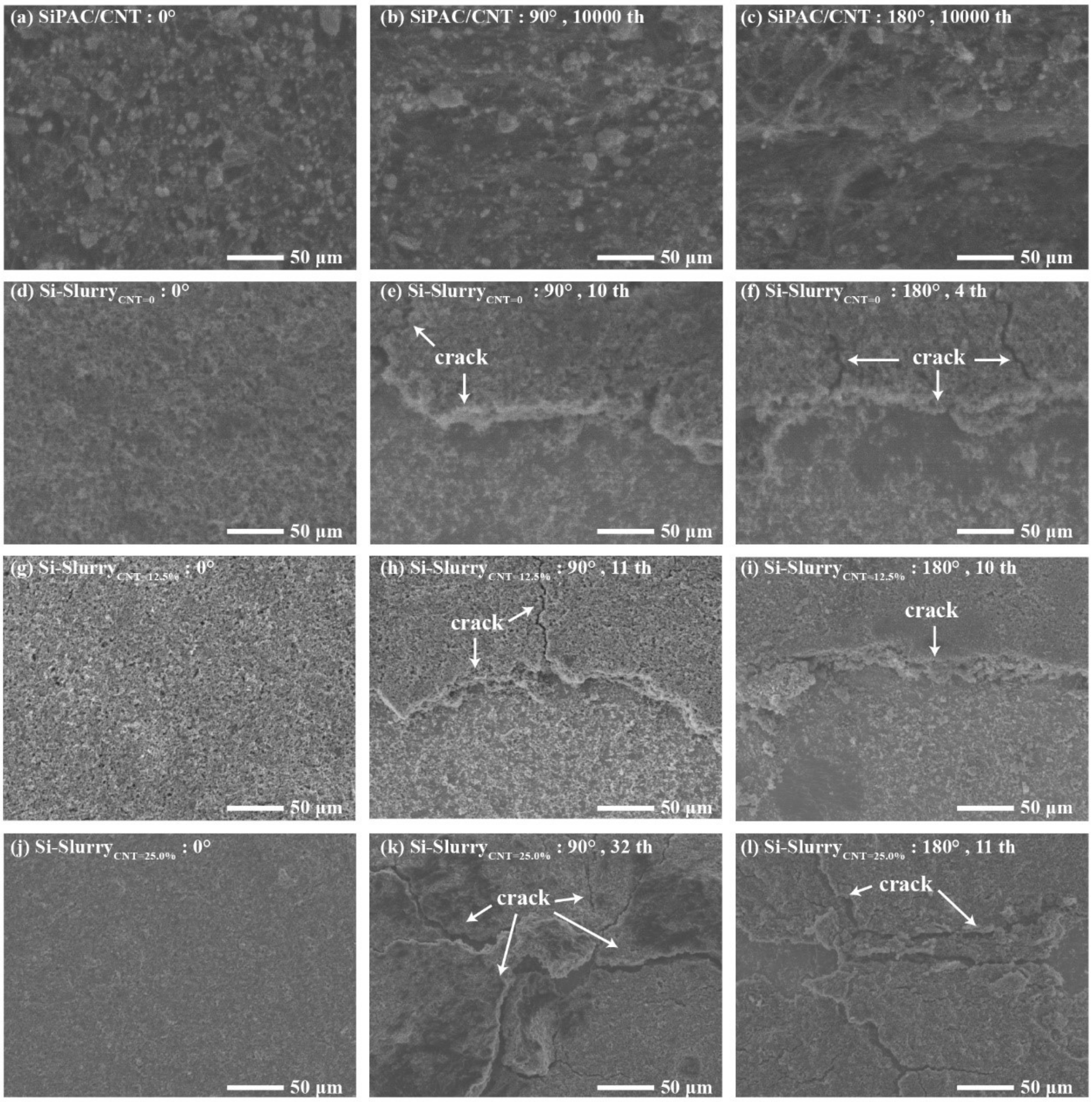

Fig. S18 SEM images of the top surfaces of the SiPAC/CNT, Si-Slurry$_{CNT=0}$, Si-Slurry$_{CNT=12.5\%}$ and Si-Slurry$_{CNT=25.0\%}$ strips before and after 90° and 180° bending.

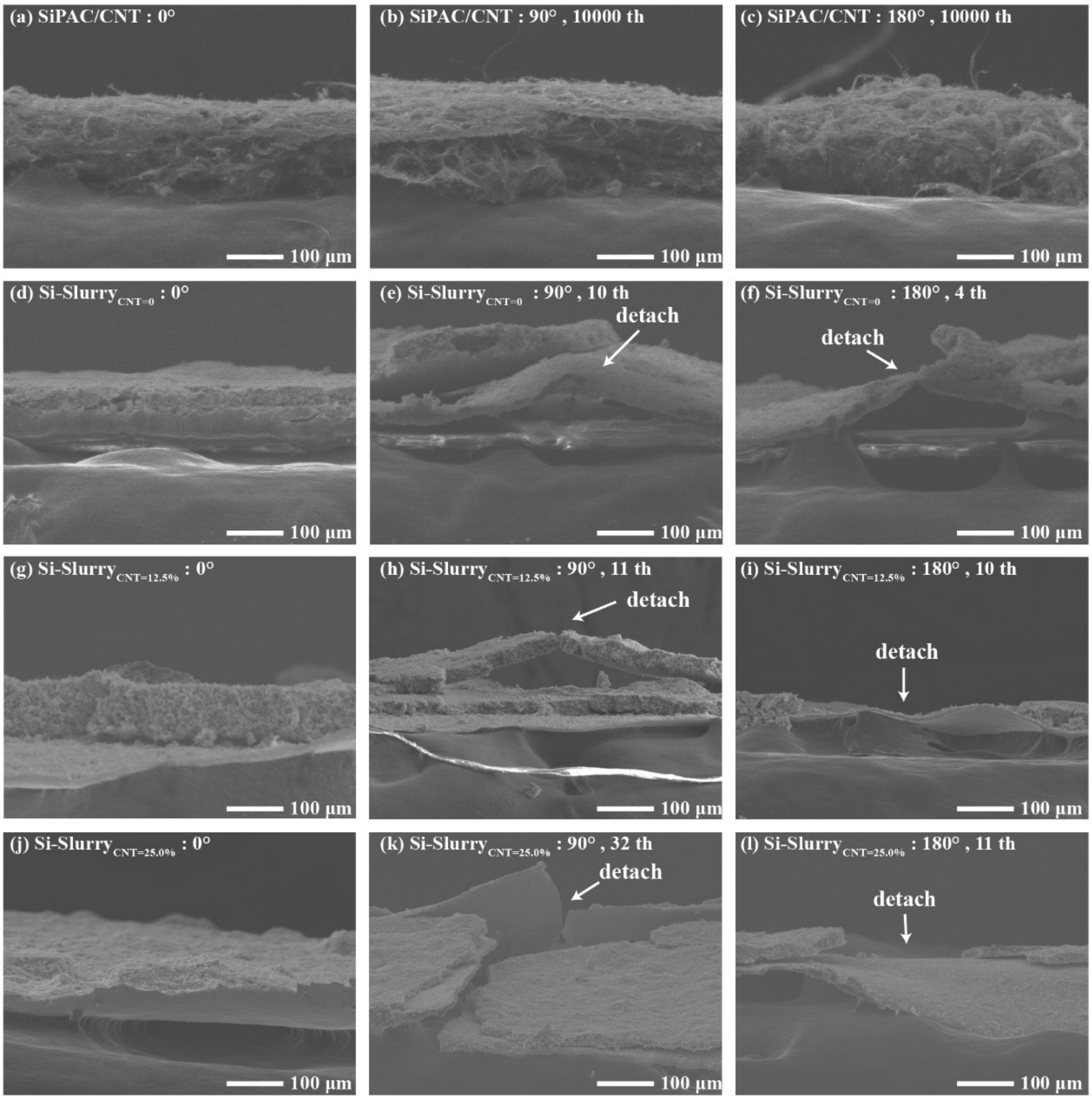

Fig. S19 Cross-sectional SEM images of the SiPAC/CNT, Si-Slurry$_{CNT=0}$, Si-Slurry$_{CNT=12.5\%}$ and Si-Slurry$_{CNT=25.0\%}$ strips before and after 90° and 180° bending.

The surface (Fig. S18a) and cross-sectional (Fig. S19a) morphologies of the SiPAC/CNT strip before bending reveal that SiPAC is uniformly dispersed in the three-dimensional porous CNT network. After bending the SiPAC/CNT strip at 90°10,000 times, a slightly raised crease can be seen on the surface (Fig. S18b) and cross-section (Fig. S19b), but the structure is still integrated. The SiPAC/CNT strip exhibits a more obvious crease after 10,000 bends at 180° (Fig. S18c, Fig. S19c), but the structural integrity is still preserved.

SEM images of the surface and side of the Si-slurry$_{CNT=0}$ sample before bending, after 10 times of 90° bending, and after 4 times of 180° bending are shown in Fig. S18e-f and Fig. S19e-f, respectively. The Si-slurry$_{CNT=0}$ sample cracks in several places and detaches from the copper current collector after a few bends. After adding CNT to the slurry, both Si-slurry$_{CNT=12.5\%}$ and Si-slurry$_{CNT=25.0\%}$ suffer from cracks (Fig. S18h, i, k, l) and detachment from the copper current collector (Fig. S19h, i, k, l).

Fig. S20 Optical photo of a SiPAC//LFP pouch cell after 90° bending for 10,000 times.

References

1 S.O. Vilela, M.A. Soto-Oviedo, A.P.F. Albers and R. Faez, *Mater. Res.*, 2007, **10**, 297–300.

2 L. Xiao, Y.H. Sehlleier, S. Dobrowolny, F. Mahlendorf, A. Heinzel, C. Schulz and H. Wiggers, *Mater. Today Proc.*, 2017, **4**, S263–S268.

3 N. Liu, X. Mamat, R. Jiang, W. Tong, Y. Huang, D. Jia, Y. Li, L. Wang, T. Wågberg and G. Hu, *Chem. Eng. J.*, 2018, **343**, 78–85.

4 Y.C. Zhang, Y. You, S. Xin, Y.-X. Yin, J. Zhang, P. Wang, X. Zheng, F.-F. Cao and Y.G. Guo, *Nano Energy.*, 2016, **25**, 120–127.

5 Y. Sun, J. Lopez, H.W. Lee, N. Liu, G. Zheng, C.L. Wu, J. Sun, W. Liu, J.W. Chung, Z. Bao and Y. Cui, *Adv. Mater.*, 2016, **28**, 2455–2461.

6 F. Di, N. Wang, L. Li, X. Geng, H. Yang, W. Zhou, C. Sun and B. An, J. *Alloys Compd.*, 2021, **854**, 157253.

7 B.H. Park, J.H. Jeong, G.W. Lee, Y.H. Kim, K.C. Roh and K.B. Kim, *J. Power Sources.*, 2018, **394**, 94–101.

8 X. Zhou, H. Xie, X. He, Z. Zhao, Q. Ma, M. Cai and H. Yin, *ENERGY Environ. Mater.*, 2020, **3**, 166–176.

9 Z. Zhang, F. Xi, S. Li, X. Wan, W. Ma, X. Chen, Z. Chen, R. Deng, J. Ji, H.J. Fan and C. Chong, *Mater. Today Energy.*, 2021, **20**, 100671.

10 K. Feng, W. Ahn, G. Lui, H.W. Park, A.G. Kashkooli, G. Jiang, X. Wang, X. Xiao and Z. Chen, *Nano Energy.*, 2016, **19**, 187–197.

11 Y. Xu, Y. Zhu, F. Han, C. Luo and C. Wang, *Adv. Energy Mater.*, 2015, **5**, 1400753.

12 P. Guan, J. Li, T. Lu, T. Guan, Z. Ma, Z. Peng, X. Zhu and L. Zhang, *ACS Appl. Mater. Interfaces.*, 2018, **10**, 34283–34290.

13 W. Zhou, J. Chen, X. Xu, X. Han, M. Chen, L. Yang and S.I. Hirano, *ACS Appl. Mater. Interfaces.*, 2021, **13**, 15216–15225.